Revision 1

Crystal shapes, triglyphs and twins in minerals: the case of pyrite

Corinne Arrouvel*

DFQM/CCTS, Universidade Federal de São Carlos, Campus Sorocaba, Sorocaba - SP, Brazil

*e-mail: corinne@ufscar.br

ABSTRACT

The euhedral shapes of pyrite FeS_2 are usually exposing three main surfaces: striated (001), smooth (111) and striated (210) leading to the cubical, octahedral and pyritohedral morphology respectively. The macroscopic striations, sometimes called triglyphs on cubic crystals, are parallel on specific surfaces and aligned to the <100> directions. Other types of striated and unstriated (hkl) surfaces can be observed on pyrite crystals from Peru, a country offering a rich diversity of shapes. A rare specimen from Elba island (Italy) is a pyritohedron with uncommon directions of striations (so-called *negative* striations, firstly described in Japanese minerals). The Wulff kinetic growth and the periodic bond chain (PBC) theories were not relevant enough to explain crystal shapes, the texture of the surfaces and twinning. To bring some new insights on crystal growth, twinning and anisotropy, pyrite samples are analyzed using XRD, SEM and EDS techniques coupled to atomistic simulations. A first analysis points out that the sulfur terminations play a key role on the growth of striations in distinguishing the six <001> directions. The *negative* striated pyritohedral pyrite would be in fact a special case that has stabilized the {120} surfaces which are structurally different from the {210} facets. The {120} surface has a slightly higher surface energy than the {210} surface (surface energies of 1.68 Jm^{-2} and 1.65 Jm^{-2} respectively, calculated with force field methods). {120} pyritohedra from Elba, Italy, are growing next to micaceous iron oxides (a type of hematite), which are also peculiar specimens with magnetic properties. Another specificity is that some rare earth elements have been identified in the pyrite sample from Elba which leads to hypothesize that geothermal conditions favor ´negative´ striations (e.g. discernible in Akita prefecture-Japan, Boyacá-Colombia and Cassandra-Greece). The striation directions become useful to distinguish (hkl) surfaces and to identify twinning as they follow the same patterns on each interpenetrated crystal. The most common twinning is the "iron-cross", a penetration twin of two crystals defined by a rotation of 90º along a [001] axis with a coincidence in the iron sub-lattice (e.g. twinning by merohedry) and with a twin center. The sulfur network also plays a fundamental role in stabilizing the (001) interface and in keeping the chemical bulk properties at the boundary, as confirmed by additional ab initio simulations. The grain boundary is a 2D defect in which the (001) twinning is relatively stable as it is a common twinning. The calculated formation energy of the rotation twinning is 0.8 Jm^{-2}. The rotation twinning is associated with an apparent reflection on (110) planes. The formation energy of the (110) mirror grain boundary is 1.7 Jm^{-2} and the interface at the atomic scale is relatively uniformed in agreement with experimental observations.

Keywords: FeS_2, crystal growth, force field, anisotropy, Fe_2O_3, Elba, geothermal

INTRODUCTION

Pyrite FeS_2 is a euhedral mineral which can adopt a wide range of different morphologies exposing some specific facets. Cubical (with 6 {001} facets) and octahedral (8 {111} facets) shapes are commonly encountered with centimetric sizes and submicrometric sizes (Rickard 2015; Wilkin et al. 1995; Folk 2005). The pyritohedron (irregular dodecahedron) is also a common shape, associated to 12 irregular pentagonal {210} facets. Other related {hk0} facets, such as {310}, {410}, {320}, {520} and {830}, have been reported by different authors (Alonso-Azcarate et al. 2001;

Murowchick and Barnes 1987; Endo and Sunagawa 1973). Many other forms of pyrite are a combination of the three main facets with truncated corners (such as truncated cube, truncated octahedron, truncated dodecahedron) with sometimes exposing other (hkl) surfaces not clearly identified. Parallel striations are common in some surfaces of minerals (e.g. pyrite, quartz, sphalerite, tourmaline, ilvaite). The striation growth has been investigated by different authors but does not converge in a unique theory. For example in quartz, Rice and Cohen suggested that the striations are from a 2D process growth (growth by layers that might be also attributed to a laminar growth) or slip lines (a 2D defect from a dislocation of a (hkl) plane from mechanical external forces). Arrouvel and Eon (2019) described the striations with a 1D process, following the favorable kinetic <100> directions. Striations are also called triglyphs, usually reported to the cubical shapes of pyrite since Gabriel Delafosse (Authier 2013) and they have been highlighted more recently onto pyritohedra (Endo and Sunagawa 1973). Endo (1978) has detailed morphologies and surface textures of a broad variety of pyrite crystals from Japanese mines. The reader will find descriptions of shapes in Dana (1903) and a wide range of indexed (hkl) surfaces (up to 81 facets) in Goldschmidt (1890). Interestingly, some rare specimens from Japan and Italy have uncommon directions of striations onto pyritohedral surfaces, suggesting a growth along <001> directions, being the most favorable directions for the kinetic growth (Arrouvel and Eon 2019). Endo and Sunagawa (1973) have called *positive* and *negative* striations to distinguish the two phenomena but up to now, no one has explained the origin of this difference.

With the recent acquisition of rare pyritohedra with negative striations from Elba island, Italy, and different specimens from Peru, a new interpretation of exposed facets, crystal growth and twinning is based on the observation of triglyph directions coupled to force field simulations. Some minerals are experimentally characterized with XRD (x-ray diffraction), SEM (scanning electron microscopy) and EDS (energy dispersive spectrometer). Simulations enable a description of structural properties (e.g. Fe/S surface terminations, interface) and energetic (e.g. attachment energy, surface energy and grain boundary energy).

METHODOLOGY

Experimental methodology

The minerals have been cleaned with isopropanol and grounded in an agate mortar. X-Ray Diffraction (XRD) patterns were obtained using a PANalytical X'Pert Pro X-ray diffractometer with a CuKα1 radiation source (wavelength λ of 1.5406 Å) and operating at 40 kV with a current of 40 mA. The sample holder was a silicon zero-background which is adequate for small amounts of specimens. The scans were performed in the angular range $2\theta = 5\text{-}90^{o}$ with steps of 0.0167° and a counting time per step of 8 s.

Most of the samples were examined on a JEOL JSM-7100F FE-SEM with FEG source of electrons (at CBPF), at an acceleration voltage of 15 kV for all measurements, in mode of collecting secondary electrons. The working distance was kept at 15mm. The elemental composition was determined using energy dispersive X-ray spectroscopy (EDS) Oxford (SDD of 80 mm^2). Magellan-FEI SEM microscope (at INMETRO) operates with secondary electrons in beam convergence mode. The images have been obtained at a voltage of 10 kV for the cubic pyrite. The working distance of the sample was 4 mm. EDS measurements are done with a voltage of 30 kV.

Atomistic simulations

Surfaces and interfaces are simulated using the program METADISE (Minimum Energy Techniques Applied to Dislocation, Interface, and Surface Energies, Watson et al. 1996). The same methodology has already been successfully employed by Arrouvel and Eon (2019) and de Leeuw et al. (2000). Atomistic simulations are based on Born model (Born 1957). The force field combines Coulomb interactions and Buckingham potential following the relation:

$$V_{r_{ij}} = \sum \frac{1}{4\pi\varepsilon_0}\frac{q_i q_j}{r_{ij}} + A_{ij}\exp\left(-r_{ij}/\rho_{ij}\right) - \frac{C_{ij}}{r_{ij}^6} \tag{1}$$

With q_i and q_j the charges on each ion i and j, r_{ij} the distance between the ions and A_{ij}, ρ_{ij}, C_{ij} are ion-ion parameters in the Buckingham potential.

The spring potential for the S_2 dimer is according to the relation:

$$\phi_{ij}(r_{ij}) = \frac{1}{2}k_{ij}(r_{ij} - r_0)^2 \tag{2}$$

with k_{ij}, the fqirce constant, r_0 the separation between the two atoms at equilibrium.

The relation for the 3-body S-S-Fe angular bond is:

$$\phi_{ijk}(r_{ijk}) = \frac{1}{2}k_{ijk}(\theta_{ijk} - \theta_0)^2 \tag{3}$$

With k_{ijk}, the force constant, θ_0 the angle between the three atoms at equilibrium.

The force field parameters are listed in Table 1.

(hkl) surface terminations are generated automatically using the Tasker approach (Tasker 1979). The choice of the surfaces has been done in priority from observed surfaces, including possible XRD extinguished peaks. Most stable terminations are reported with their attachment energies and their surface energies. The attachment energy, energy released per mol by the growth of a layer (or slice) of thickness d_{hkl} (interplanar distance), is expressed as:

$$E_{hkl}^{att} = E_{bulk} - E_{slice} \tag{4}$$

With E_{bulk} the lattice energy of the crystal, E_{slice} the energy of the (hkl) slice per mol.

The surface energy in vacuum, γ_{hkl}, for the (hkl) surface of the crystal is as follows:

$$\gamma_{hkl} = \frac{E_{hkl} - N.E_{bulk}}{A_{hkl}} \tag{5}$$

With E_{hkl} the energy of the (hkl) surface, E_{bulk} the energy of the bulk normalized to the number N of units in the surface, A_{hkl} the surface area.

Contact mirror twins are simulated for this study. The unrelaxed slab is reflected and scanned in moving its position to the respect of the other slab by steps of 0.2 Å along the 2 dimensions of the (hkl) interface plane. At each point of the grid, the system is relaxed. The lowest interface potential energy E_{GB} gives the most stable grain boundary per surface area. From E_{GB}, the formation energy (E_f) and the cleavage energy (E_c) are calculated using the relations $E_f = E_{GB}-E_{bulk}$ and $E_c = 2E_{slice}-E_{GB}$.

To stabilize a grain boundary, the E_f is minimized and its E_c is maximized.

Those gliding mirror twins are more easily identified by HRTEM (high-resolution transmission electron microscopy) while rotating twins forming penetrating twins are deduced by macroscopic observations.

The morphology of a crystal minimizes the surface energy of a fixed volume. The shape is constructed using the Wulff construction (Wulff 1901) in which the ratio between the energies of (hkl) planes, γ_{hkl}, and the distances from the mass center, h_{hkl}, of the solid is a constant α:

$$\frac{\gamma_{hkl}}{h_{hkl}} = \alpha \qquad (6)$$

The Tasker´s notation (Tasker 1979) is used in the text to classify each type of termination of (hkl) surfaces. The notation distinguishes three types of surfaces in ionic solids. Type I and type II are from nonpolar stoichiometric slabs while type III is from a polar slab. In type I, each plane is electrically neutral. In the case of surfaces type I in pyrite, the amount of ferrous cations and pairs of persulfide anions is igual. In type II, each plane is charged but the dipolar moment perpendicular to the surface is null. In that case, pyrite can be Fe-terminated or S-terminated. Type III stands for polar surfaces which tend to be stabilized by reconstruction to cancel the dipole moment.

RESULTS

Observed minerals

A special interest is to describe the morphologies, striations and twins to common and rare specimens. Some minerals come from Peru, country which has the reputation of offering the most varied shapes of pyrite (in particular in Ancash). The three main shapes are introduced and characterized: the cube, the pyritohedron and the octahedron (the mineral photographs in Fig. 1,2,3 are from Arrouvel´s private collection). One sample is a kind of transformation of pyritohedron to cube (or vice versa) which corresponds to an intermediate shape (h10), with h > 2 (Supplementary Information Fig. SI1). This sample presents as well some anisotropies that will be discussed later. Smooth planes are visible and correspond apparently to (310) facets (see Fig. SI1). In general, the striations are observed on cubical and pyritohedral morphologies. It appears that they are also directional, implicating that the six <h00> directions of growth are in fact distinguishable. This textural anisotropy can be noticed in many minerals with the naked eye. The directions of growth are highlighted in the SEM image of the cubical pyrite in Figure 1. The EDS analysis identifies other impurities at the surface, Mg, Al and Si on this sample. The quantities of those elements are of the order of few % and traces of some transition metals (Cu, Mo, Zn, Co) can be detected but the EDS technique is not relevant enough to consistently characterize all the samples and their surfaces as the quantities vary considerably.

XRD spectra bring some information in verifying the purity of samples and the possible existence of other phases. Indeed, the cubical pyrite presents some inclusions of vaesite NiS_2 (see XRD peaks in Figure 4). Two other peaks at 51º and 62º from impurities do not belong to vaesite. Those peaks have been attributed to {106} and {304} planes of troilite FeS impurities by Vedavathia et al. (2015). We note that troilite is a rarer native mineral, usually found in meteorites (Skala et al. 2006 and references therein). Rare specimens from Elba (Tuscany, Italy) are pure pyrite pyritohedra with clear *negative* striations (Fig. 2). On this specimen, the directions of growth are net while the texture is more irregular on analogous Japanese samples (Endo and Sunagawa 1973). Furthermore, unmistakable textural anisotropies are also discerned onto each pair of striated surfaces (e.g. (201) and $(20\overline{1})$ are then considered chiral through the optic (100) plane). The *positive* striations onto a common pyritohedron are highlighted in Figure 2; this mineral is from Peru (n.b.: it is the same sample shown in Arrouvel and Eon (2019)). Some nickel and aluminium impurities are identified by EDS on the sample (an example of measurement: atomic concentration Fe 23%, S 55%, Ni 2% , Al 3% ; titanium, sodium, magnesium might also appear in some measurements as traces; carbon and oxygen are with higher concentrations). On octahedra, <h00> striations are visible onto other types of facets, in particular at the intersections of {111} facets (Fig. 3). In addition, this mineral from Peru is having some extra minor smooth facets and a rare twin. The striations have been amplified by SEM techniques. Another interesting remark is that the XRD (001) peak becomes less intense than the (210) peak on the negative sample (Fig. 4). The origin of the striations and the characteristic of the twins will be further discussed after the calculation section.

Further observations on morphologies and textures are from mineral museums (Geosciences Museum of USP-São Paulo Brazil; the Science and Earth Museum in Urca-RJ Brazil; Mineral Museum Andres del Castillo, Lima Peru) or published work (Murowchick and Barnes 1987, Alonso-Azcarate et al. 2001; Couderc et al. 1980). The examination of dodecahedra brings important information. Indeed, regarding the striated patterns, two types of pyrite can be distinguished on a pyritohedral morphology as defined by Endo and Suganawa (1973): the negative pyrite striations and the positive pyrite striations (Fig. 2). Singularly, another type of dodecahedron (rhombic dodecahedron) with the pyrite crystal structure has been successfully synthesized by Yang et al. (2009); it is an NiS_2 particle with {110} facets. Up to now, no such dodecahedron of FeS_2 crystal has been found. Some icosahedral crystals, considered rare for collectors due to an apparent

5-fold symmetry of the shape, have been mistaken with morphologies exposing {111} and {210} facets (Arrouvel and Eon 2019) in which the presence of striations in some specific surfaces (i.e. {210} facets) should confirm this fact. They should be called pseudo-icosahedra in that case, exposing two types of (hkl) surfaces.

Pyrite often grows next to other minerals (e.g. sphalerite, quartz, calcite). The pyritohedral pyrite from Elba grows in contact with specular hematite. This layered hematite Fe_2O_3 is a specimen called micaceous iron oxide (MIO) with magnetic properties (the extracted sheet is attracted by a common magnet which indicates the existence of a strong magnetic field). Natural micaceous hematite can be associated with pyrite (Benvenuti et al. 2013) and its hydrothermal synthesis forming hexagonal flakes can be done from pyrite and iron hydroxide (Liu and Zheng 2011). In SI (Fig. SI2), the reader will find the XRD spectrum and the SEM image of MIO with striations aligned along a and b axes in the hexagonal system (forming an angle of 120º). As the phase is pure (without detecting other phases or compounds such as magnetite), this uncommon magnetism is related to hematite (an investigation to explain the crystal growth, striations and magnetic properties of MIO hematite coupled to simulations is under progress). The (001) surface is the basal one (hematite defined in the hexagonal unit cell, space group number 167, $R\overline{3}c:H$), with the lowest attachment energy (unpublished results). Another unusual finding is that traces of rare earth elements (REEs) have been spotted in pyrite (e.g. Pr, Nd, Pm). However, the concentrations are at the detection limits for EDS and ion mass spectroscopy will be necessary for such a specific study. Furthermore, the FeS_2 surfaces seem to be oxidized due to the high concentration of oxygen which limits as well a careful analysis of other metal impurities (Ni, Mo, Zn). Some studies have detected rare earth elements in compounds from Elba (Saccani and Principi 2016; Squadrone et al. 2018) which reinforce this particularity. No REE has been identified in hematite with EDS while Lippolt et al. (1995) reported an analysis using mass spectroscopy, photometer and helium decay to estimate the concentration of U, Th and Sm elements in hematite specularite (another term to define shinny hematite) from Elba. No study on rare earth elements has been reported in the Japanese samples from Endo and Sunagawa (1973) so no correlation based on the presence of REE impurities can be done. On the positive striated pyrite, the lines are blocks of {001} facets growing in a specific direction. EDS measurements indicated Ni, Ti and As as the major impurities (e.g. Fe (22.5%), S (54.0%), As (0.12%), Ti (0.16%), Ni (0.23%), but the atomic ratio can vary due to the heterogeneous character of minerals).

A typical truncated octahedron, origin from Peru, is displayed in SI (Fig. SI3). The {111} facets are smooth and the facets at the corners ({001} facets) have well aligned striations along the respective a, b and c axes. A small anisotropy is perceptible indicating a small inclination of the lines on each {001} facet. Another specimen from Peru is detailed in Figure 3, with various crystals interpenetrating. This sample is octahedral, not truncated by {001} facets but exhibiting other ones at the edges and corners. Besides, an uncommon {111} twinning is also noticeable. In this pyrite, some traces of Pt and Zn on the (110) surface are measured by EDS (with atomic concentrations at the limit of detection of 0.1% and 0.2% have been measured for Pt and Zn; with Fe 19.3% and S 40.1%). The corners expose some facets, that are discussed later, which are likely to be {210} facets. At the edges, an asymmetry is evidenced by the exposition of a very smooth unstriated facet at only one side of the {110} striated facets. This glossy facet is even more apparent at the {111} twinned plane. A further study including goniometric measurement would be necessary to characterize this singularity. A striated facet at the edge of a small crystal co-growing on the top of {111} facet is exemplified and magnified in Figure 3. Interestingly, it is perceivable that the striations on the {110} plane are meeting at the middle of the facet. It may be a manifestation of a twinning phenomenon. Some hypotheses on texture and crystal growth are proposed in the discussion section.

Simulation of surfaces, morphologies and twins

Isotropic Pyrite belongs to the space group $pa\overline{3}$ (number 205) with the S_2^{2-} dimers orientated along the <111> directions. Anisotropic pseudocubic pyrite structures have also been reported by Bayliss (1977 and 1989) with space groups P1 and Pca21. The simulations have been done on the isotropic pyrite. FeS_2 can adopt a lot of different shapes as it has been already introduced in a surface study by Arrouvel and Eon (2019). The same methodology with classical force fields is used to simulate surfaces and interfaces. A special attention is addressed to twinning and striations. Thanks to the acquisition of rare pyrite crystals, new (hkl) surfaces have been investigated, in particular permuting Miller indices. Indeed, the {210} facets forming the pyritohedron are different from {120}. All possibilities of surfaces are revisited, including then extinguished XRD peaks.

Calculated surfaces (Table 2) are mainly type II (Fe or S-terminated) with the exception of (110) surface in which the most stable termination is type I (Fe S1-S2) (using Tasker´s notation). Attachment energies give some relevant information on the kinetic growth. The lowest energy (in absolute value) gives the surface growing faster. As it has been previously established (Arrouvel and Eon 2019), the lowest attachment energy is for the (001) plane. The most favorable growing [uvw] directions are in the following order: [001] > [110] > [210] > [310] = [130] > [120] > [111] > [311]. We note that {210} facets have been revisited and a cut has been stabilized. A key result is that the (210) surface is structurally different from the (120) surface and their surface energies are close. In Fig. SI4 are highlighted the <100> directions in which the sulfur network has a clear distinction. The second important observation is that the most stable configuration of the (210) facet is S-terminated while the (120) facet is Fe-terminated. The (120)S is not stable compared to (120)Fe, (210)S and (210)Fe. The main reason comes from surface dandling sulfur ions which are unstable entities. In increasing one Miller index, the structure and energy differences between the two types of {hk0} families are also perceptible. Indeed, the stable cut of (310) is Fe-terminated while (130) is slightly less stable and S-terminated (see Table 2).

The general trend on the relaxed surface energy order from Table 2 is: (001) < (310) < (130) < (210) ~ (110) < (120) < (311) < (111). Interestingly, the Fe-terminated (310) surface is energetically stable. The Fe-terminated (210) and (310) are shown in Fig. SI5. Their surface structures are similar (with 4-fold Fe species and dangling Fe-S bonds). The (310) surface enables a step of (001)-like termination which might explain the stabilization of the (310) surface toward the (210) slab. This surface has been rarely observed but its orientation can be part of some anisotropies in positive striated pyritohedra presented in the present paper. This surface will be then further discussed in the next section.

The orientations of the sulfur terminations onto (001) planes are directional along a, b and c axes (see the directions based on S-S orientations in Fig. SI6). The orientations backward and forward have been already noted by de Leeuw et al. (2000). Simulated STM images using ab initio methods clearly show parallel [001] lines formed by the sulfur network (Arrouvel 2021). The same topology has been evidenced by an STM simulation of marcasite {101} (Dzade and de Leeuw 2017). The epitaxial relationship between sulfur-terminated surfaces favors the overgrowth of the two dimorphs and the same relation is auspicious for mirror and rotating twinning as discussed later.

Regarding the sulfur network, it becomes also possible to distinguish the two types of pyritohedra. The {210} pyritohedron is defined with the lines on the (001) surface oriented along the b direction, giving the positive striated case. This pyritohedron is then made of (210), $(\bar{2}\bar{1}0)$, $(\bar{2}10)$, $(2\bar{1}0)$, (102), $(\bar{1}0\bar{2})$, $(10\bar{2})$, $(\bar{1}02)$, (021), $(0\bar{2}\bar{1})$, $(0\bar{2}1)$ and $(02\bar{1})$. The negative case is {120} pyritohedron, made of: (120), $(\bar{1}\bar{2}0)$, $(1\bar{2}0)$, $(\bar{1}20)$, (201), $(\bar{2}0\bar{1})$, $(\bar{2}01)$, $(20\bar{1})$, (012), $(0\bar{1}\bar{2})$, $(01\bar{2})$ and $(0\bar{1}2)$. The <001> directions of the striations are in complete agreement in discriminating the two types of pyritohedron (see Fig. SI6).

The orientation of the striations follows the same rule in twinned crystals (some examples of unstriated and striated twinned morphologies are illustrated in Fig. SI7 and Fig. SI8). As a matter of fact, it has always been reported that two pyritohedral interpenetrating crystals (twin called cross of iron), in which the axis of rotation of 90º on the central axis [001], conserve the orientation of striations (negative and positive iron-cross pyrites are exposed in the museum of minerals in Sorbonne University, Paris, France and many other twinned minerals are accessible online such as mindat.org). Using the notation of Aoki and Nakamuta (1984), the penetration twin is then $[100]_{90^{\circ}}$. This type of twinning is by merohedry, as defined by Friedel (1926). In cubical and octahedral morphologies, the perfect $[100]_{90^{\circ}}$ twin axis does not allow visualizing twinning on the simulated morphologies. In natural minerals, some anisotropies are commonly reported and it is possible to observe $[001]_{\sim 90^{\circ}}$ as a twinning axis in the cubical morphology (see Fig. 2c from Alonso-Azcarate et al. (2001) illustrated in Fig. SI7b and see Pabst 1971).

Another type of twinning based on geometrical observations is also recognizable connecting a (110) plane with a (010) plane. To connect those two planes, there is a mismatch along one direction. This phenomenon explains as well the direction of the striations perpendicular to the edges (the (110) plane adopting the direction of striations of the (010) surface). On cubical pyrite crystals (typical samples from Spain), the contact plane is recognizable using rotations of 45º. Striations have been added in Fig. SI8 respecting the rotation laws. Fig. SI8a illustrates this kind of contact twin in which the twin rule is a rotation of 45º on the [001] axis, noted $[001]_{45^{\circ}}$. The planes in contact are (100) with $(\bar{1}10)$. In order to consider the epitaxial relationship between (100) and $(\bar{1}10)$ planes, the simulated surface energy ratio between the two twisted cubes is of 1.41 ($\cong\sqrt{2}$ to better verge on the merohedral rule on the coincidence contact rectangle and then some defects are expected at the atomic scale interface due to the irrational ratio). In octahedra, the same type of twinning is happening when the edge (e.g. (110) plane) of secondary crystal grows at the corner of the primary crystal (e.g. a (100) plane). This case is illustrated in Fig. SI8b (nb: the simulated surface energy ratio between of the two schematized octahedra is $\sim\sqrt{2}$). When the twin rule is applied two times (i.e. $[001]_{45^{\circ}}$ and $[010]_{45^{\circ}}$) onto the respective cubical pyrite crystals (see Fig. SI8c with a simulated surface energy ratio of $\sim\sqrt{3}$), the (001) plane of the bigger crystal is in contact with the (101) plane of the smaller crystal. In applying a rotation of 45º on [110], the cubes are likely to grow at the common corner (see Fig. SI8c). Another type of rare twinning involves a {111} plane. Such type of twinning is highlighted in Figure 3 (pyrite sample from Peru). No rotation rule has been evidenced due to the lack of information, part of the twinned plane being a bulk. Apparently, the initial triangle of the exposed (111) plane is doubled along one facet and forms a lozenge. No intersection is visible with the naked eye on the facet interface.

To remain closer to realistic boundaries, DFT simulations have been undertaken for the rotational $[001]_{90°}$ twinning and force field simulations on glide mirror twins for (110) and (111) interfaces. Indeed, the most common reported twin is the rotational twin along [001] direction which has also been associated with the {110} contact twin, perceivable by HRTEM (Recnik et al. 2016).

VASP software is used for DFT calculations (Kresse and Furthmüller 1996). RPBE+D3 functional and PAW pseudopotential are employed with a cutoff energy of 500 eV, a k-points grid of 12×12×12 for the bulk and 12×12×1 for the (001) surface. The convergence criterion is 10^{-5} eV per cell on the energy and less than 0.02 eV/Å on the atomic forces for the ionic relaxation. Additional DFT simulations have been done to include twinning in the present study. The S-terminated slab is the most stable, with a surface energy of 1.19 $J.m^{-2}$ (slab thickness of 14.8 Å and a vacuum thickness of 13.2 Å) which is in agreement with other DFT studies (Hung et al. 2002b; Alfonso 2010). The (001) slab has 6 layers and half of the slab has been rotated by 90º (see Fig. SI9). With this transformation, the twinned slab is stable and uniform. The grain boundary energy in the slab (SGB) is the difference between the twinned slab and the untwinned slab per surface area. E_{SGB}=0.8 Jm^{-2}. The same value has been found in twinning a bulk supercell (1×1×4). The calculated Bader charges q of S and Fe at the surface are not really modified from the bulk values. A small disproportionation of the charges in the bulk is noticeable for the sulfur species, q=-0.38 and q=-0.33. A slight reduction of the charge is on the subsurface sulfur atoms, q=-0.40. In the bulk, the iron has a charge of +0.70. At the surface of the slab, the charge slightly increases reaching q=+0.74.

Contact twins are simulated with METADISE. Some tilted configurations might appear stable with a negative energy formation but they are linked to some deficiencies with the force field method in which strong reorganizations of the surface chemistry is not considered. Indeed, some surface energies are overestimated with force fields compared to DFT simulations because the change on the oxidation state of the species is not considered (e.g. the (111) surface of pyrite FeS_2 and the (110) surface of marcasite FeS_2 which are surfaces perpendicular to S_2^{-2} dimers. See Arrouvel 2021). The formation of vacancies at the boundary and steps/kinks are part of strong reorganizations of the ions at the interface and such grain boundaries are expected to be destabilized. Realistic models are likely to be uniformed and strongly reconstructed minima are then disregarded since force fields is not adapted for such cases. The optimized (110) grain boundary is in Figure 5a. The mirror slab (Tasker type I) has been displaced by 0.2 Å and 0.2 Å on the two lattice directions parallel to the (110) plane (in the bulk, the optimized lattice parameter is a=5.48 Å). The formation and cleavage energies are $E_f = 1.73\ Jm^{-2}$ and $E_c = 2.39\ Jm^{-2}$. The most stable Fe-termination of the (111) surface has been mirror twinned. The displace at 1.0 Å and 0.4 Å is rather uniform and the formation energy is negative, $E_f = -3.59\ Jm^{-2}$. The cleavage energy is relatively high, at $E_c=10.01\ Jm^{-2}$. Results from force fields indicate then wrongly that the (111) grain boundary is favorable due to the initial overestimation of the surface energy of the (111) surface. Undoubtedly, this surface is reconstructed, goes through chemical changes that have not been considered with force field methods. From DFT and force field calculations, the grain boundary formed from the $[001]_{90^\circ}$ rotation is the most favorable twinning, with a lower formation energy. For a consistent comparison, DFT calculations will be undertaken in a future work to verify reconstructions, non stoichiometric interfaces and rotational twinning of other (hkl) grain boundaries.

DISCUSSION

The morphology and texture of minerals are modified regarding external conditions involving thermodynamic and kinetic mechanisms. Various geological mechanisms can lead to the formation of pyrite such as precipitation under hydrothermal conditions (from Fe^{2+}(aq), FeS and Fe_3S_4 precursors for example), metamorphism (from oxide precursors, Arrouvel and Prinzofer 2021) and volcanic activities under sulfur conditions (e.g. iron-rich compounds in basaltic magma). The rate of pyrite formation depends on many factors (e.g. temperature, concentrations, pressure, precursors, catalysts). Twinning is also a phenomenon still in debate in which the laws obey thermodynamic, structural factors. The present paper discusses on thermodynamic and kinetic aspects at the atomic scale, based on energy minimization of surfaces and twins. Lowest energy systems are then expected to be more common. Considering that penetration twinning should embrace a law independent of the shape of the single crystal, it becomes important to verify the validity of the law not only on pyritohedral pyrite but also on cubical and octahedral pyrite combining simulations and experimental observations.

Thermodynamic factors on crystal growth

The ratio [Fe]/[S], the temperature and the aqueous conditions are factors undoubtedly controlling the morphology as demonstrated by simulations and syntheses in laboratories. The {001} facets are thermodynamically stable. At higher Fe content, cubical shapes are dominant and often referred to FeS as a precursor. Troilite FeS has been characterized in the cubic sample (Fig. 4). The cubical morphology of pyrite and troilite are favored at higher temperature. The simulations indicate that the stoichiometric FeS_2 {001} facets are sulfur-terminated. At high sulfur content, the octahedral morphology of iron pyrite prevails. The stoichiometric {111} facets are iron-terminated (Barnard and Russo 2009; Alfonso 2010; Liu et al. 2014; Zhang et al. 2015). The pyritohedron is stabilized under intermediate conditions and under aqueous conditions (Barnard and Russo 2009). The pyrite from Elba seems to have grown under high Fe content. Indeed, the island has been over-exploited for centuries for iron ores. The rare *negative* striated pyrite is found in Rio Marina, Elba, with hematite-rich ores such as MIO/specularite and with ilvaite (Savage et al. 2008; Benvenuti et al. 2013; Lippolt et al. 1995; Tanelli et al. 2001 and references therein). Another characteristic is that Rare Earth Elements (REEs) have been identified in Elba (Saccani and Principi 2016; Squadrone et al. 2018). Negative striated pyrite crystals were formerly poorly described and characterized. The sample of pyrite from Elba contains REEs which is consistent with geological data. Impurities are factors that can influence the shape and texture of particles however, up to now, no study can affirm it. The negative striations have been reported by Endo and Sunagawa (1973) in the Japanese mines and their origins were unsolved. Curiously, at the surface of pyritohedral pyrite from Boyacá (Colombia) and Cassandra (Greece), negative striations can be recognized (see mindat.org), however, to my knowledge, this observation has never been commented in the literature and field studies would be essential to better correlate morphology and crystal growth regarding common geological characteristics in Eastern Elba (Italy), Akita prefecture (Japan), Boyacá (Colombia) and Cassandra (Greece) (i.e. volcanic complexes/geothermal systems (Zucchi 2020; Endo 1978; Noorollahi et al. 2007; Alfaro 2005; Alfaro-Valero et al. 2020; Kougoulis et al. 2007) enriched with REEs).

Different theories on crystal growth can be referred to striations. For example, the Periodic Bond Chain (PBC) and Hartman-Perdok theories (Hartman, 1963; Hartman-Perdok 1955) define stepped, flat and kinked surfaces based on the attachment of building units. However, those theories are incomplete to explain the different shapes and textures on the surfaces, as already observed by Endo and Sunagawa (1973) and Endo (1978). In the case of pyrite, the building units are made of {001} facets which are considered flat surfaces in the PBC theory. The fact to observe specific growing directions onto {001} facets means that striated {001} surfaces are not so-called ´flat´ surfaces. Furthermore, there are apparently two different growth mechanisms onto {210} facets with positive and negative striations, described as stepped and flat respectively by Endo and Sunagawa (1973).

Up to now, no rational models or causes had been able to explain the difference between the two types of pyritohedra. The presence of cobalt is the only element reported by the authors as an impurity that might be at the origin of the striation growth mechanism on the negative pyrite. However, cobalt is a common impurity in pyrite from other localities (Savage et al. 2008). Purmice tuff is notified in the Japanese mines, they have usually high content of hematite. Further chemical and structural analyses including the verification of the presence of REEs, iron ores content on Japanese samples would be necessary to correlate the specificity of the geological conditions. Other studies report that pyritohedra appear at higher S content (Murowchick and Barnes 1987; Alfonso 2010; Barnard and Russo 2009, Alonso-Azcarate et al. 2001). Usually pyritohedra are referred to *positive* striated one and can co-growth with cubic shapes. Some pyritohedra are flatten with intermediates (hk0) planes, increasing h index leads to the cube.

Kinetic factors on crystal growth

Natural crystals manifest morphological, surface and/or optical anisotropies. A previous study suggested that the textural anisotropy from the striations is due to a kinetic effect (Arrouvel and Eon 2019). The <001> directions are kinetically favored, the attachment energy being the lowest on the {001} facets. The growth rate has been reported higher for the (001) surface, of 1 mm per day (Yamada 1979), which strengthens the role of kinetic and striations in pyrite growth. The <001> striation directions explain as well the difference between the two types of pyritohedra, exposing {210} or {120} planes. We note that the XRD (120) peak is extinguished following the selection rules (extinction of the peaks for h odd in (hk0); k odd (0kl), l odd (h0l)), surface regularly ignored in previous studies. The striations are also unidirectional, noticeable by electron microscopy on cubical pyrite. The mechanism is likely to be determined by the orientations of the dimers on each surface.

One of the three a,b,c directions can even dominate which is defined as a 1D mechanism for the growth of nanowires, nanorods observed by Cabán-Acevedo et al. (2012 and 2013) and acicular (rare specimens are from Naica mines, Chihuahua, Mexico, exposed in the museum of Sorbonne University, France and White 1973), dentritic pyrite (Murowchick and Barnes 1987). The whisker synthesized by Yamada et al. (1979) is also a growth along one <001> direction, with the directions of striations confirming it, and the extremity of the whisker is made by {111} facets.

Simulations have been done on marcasite FeS_2 using the same force field (Arrouvel 2021). Marcasite is a metastable polymorph, rarer than pyrite, growing at low temperature and low pH (Murowchick and Barnes 1986; Schoonen and Barnes Barnes 1991; Drabek and Rieder 2005; Zavrazhnov et al. 2018; Rickard 2012; Gronvold and Westrum 1976; Sun et al. 2011). The lowest attachment energy of marcasite is for the (010) surface (-0.20 eV/atom, almost identical to the (001) surface of pyrite) and the most stable surface (i.e. with lowest surface energy) is the (101) surface with a topology similar to pyrite (001). Even if the single crystal morphologies are very different between marcasite and pyrite, the most favorable kinetic growth is linked to the striation directions for both polymorphs.

The growth of pyrite nanoplates (Cabán-Acevedo et al. 2013) follows the same process in 2D. Natural pyrites exhibit as well shapes elongated on 1 or 2 <100> directions (some distorted cubical and pyritohedral minerals are reported in Alonso-Azcarate et al. 2001). Another type of anisotropy is distinguishable on the striations of the pair exposing {2±10} planes in some pyritohedral crystals. One of the facets gets lines apparently more flat, tilted close to roughly 20º but goniometric measurement would be necessary to verify if the angle corresponds to the (310) plane. The smooth facet (more neatly visible in the sample in SI1) is also linked to a reduced symmetry of the pyrite. Indeed, the (310) facet appears in one pentagonal facet of the pair, meaning that the $(3\bar{1}0)$ facet is not equivalent to the (310) facet. The fact that (310) surface is flat while (210) surface is stepped seems also to question the PBC and Hartman-Perdok theories. At the atomic scale, the difference from the two surfaces is that the most stable cut under vacuum of the calculated (310) surface is Fe-terminated while (210) surface is S-terminated. S_2^{2-} dimer is the leading factor that can explain consistently the striation directions on S-terminated stepped surfaces. We note that the striated faces correspond also to faces with optical anisotropy (Gibbons 1967).

Another information extracted from attachment energies enables the interpretation of oriented attachment (OA) growth. Nanoparticles, referred as quantum dots (Gong et al. 2013), should orient spontaneously and be attached through the {001} facets in order to form a squared nanosheet or a cubical nanoparticle. Yu et al. (2015) did report that the solvent 1-octylamine plays as well a role in the OA mechanism and kinetic mechanism through the {001} facets. The final shape is driven by the thermodynamical equilibrium. Surface energies under vacuum obtained with force fields give a relevant order of stability but the method presents some limitations. Indeed, terminations with cut dimers should induce reduction and oxidation of the surface species (e.g. formation Fe^{3+} and S^{2-} as it has been suggested by Nesbitt et al. (1998) using XPS experiments). The (111) surface appears to be stabilized when it is studied with ab initio methods (Hung et al. 2002a; Alfonso 2010). Another way to stabilize a surface is to build steps made of the stable one. It is the case of the (110) surface which can be steps of {001} facets (Hung et al. 2002b; de Leeuw et al. 2000). Steps of {001} facets have been observed onto natural minerals at the macroscopic size on some (110) planes, analogously of striations onto (210) planes. In Figure 3, the mineral enables the visualization of the major flat (111) surfaces and the striated (210) and (110) surfaces. Typical observed morphologies (of samples from Peru) exposing those facets are schematized in Figure SI10.

While the striation directions follow concerted <100> directions in the negative pyritohedral pyrite, the striations in the {120} pyritohedron might be described as a 2D process (e.g. layers of (010) planes growing along the b axis visible on (012), $(0\bar{1}2)$, $(01\bar{2})$ and $(0\bar{1}\bar{2})$ facets - using the convention of the directions shown in Fig. SI6). We note that the construction of the {120} pyritohedron is obtained by a $[100]_{90^\circ}$ rotation of the {210} pyritohedron.

Grain boundaries: mirror and rotational twinning

Twinning is another important phenomenon in mineralogy giving some difficulties of interpretation in X-ray crystallography and crystal growth. Iron network is a sub-lattice leading the twin laws in which the geometry matches at the interface. Sulfur atoms are expected to play a role in grain boundaries. From the simulations, the (001) interface is the most favorable grain boundary, having a lowest formation energy with a minimal distortion of the sulfur network at the interface. This type of twinning is expected to be the most frequent in pyrite. The rotation of 90º along the [001] axis reduces the symmetry of the crystal at the atomic scale in changing the orientation of the sulfur network (see Figure SI9). The lowering of the cubic symmetry has already been identified by Fedorov and attributed to the orientation of the sulfur atoms (Rickard 2015). The external structure of twinned crystals keeps well-defined facets and shapes, the center of the cube common of the 6 [u00] axis and {110} being "imaginary" mirror planes. [001] is a rotation twinning axis easily identifiable, especially in the case of iron-crossed pyritohedra with a common twin center and an external symmetry of $4/m\bar{3}2/m$ (Donnay et al. 1977). Two crystals are interpenetrating with a rotation of 90º and with the same external texture on the facets. An apparently exception comes from Endo and Sunagana (1973) who did mention that a pyritohedron from Shakanai mine presents the two types of striations. Another possibility would be that the mentioned pyritohedron is twinned but due to the lack of information, it is not possible to affirm this hypothesis. In principle, the $[001]_{90^{\circ}}$ twinning is possible on pyritohedra but also on cubical and octahedral pyrite. Indeed, the twinned cube can be visualized in Fig.2c from Alonso-Azárate et al. (2001) (schematized in Fig. SI7b) but was not described by the authors in that regard. Other iron-cross shapes are described by Pabst (1971). We note that this most common merohedral twinning has the lowest surface area of coincidence-site lattices.

The internal structure of twins induces some anisotropies and dislocations at the grain boundaries, and it can be examined experimentally by electron microscopy. The rotational [001] twinning has also been linked to contact twin (110) (Rečnik 2016). The calculated glide on the (110) interface is low hence reinforcing the possibility of a combined phenomenon. If twinning dominates, a change in the XRD spectra is expected, such as additional XRD peaks (the XRD simulation of the bulk twinned by a rotation of 90º has been done, not shown in the present paper). The chemical structure, the lattice parameters, the ionic diffusion and electronic conductivity may also be affected but up to now, no clear correlation can be confirmed. For example, Cabá -Acevedo et al. (2012) suggested that the boundaries favor the ionic diffusion during nanowire growths while in perfect whiskers, without dislocation, the growth mechanism through boundaries is excluded (Bonev et al. 1985). Huang and Meng (2007) suggested that the increase of defects decreased the conductivity in pyrite films while the increase of defects from vacancies or boundaries seemed to decrease the band gap (Roberts et al. 2019). In the present study, the calculated band gap with RPBE+D3 is 0.44 eV for the bulk (Band gap experimental being 0.95 eV, Ennaoui et al. 1993) and is almost not existing on the (001) slab, which is related to an increase of the conductivity. The results are similar to the DFT study by Hung et al. (2002b). The DOS of the twinned slab is analogous to the untwinned slab. On the twinned bulk, the band gap is 0.49 eV. In other words, the rotational twinning did not modify the electronic properties of the material and a posible change in the conductivity should come from other types of defects including surface states. We note that the DFT simulation of the rotation twinning does not represent the interpenetration of 2 crystals because only the (001) interface has been isolated.

The (111) twinning is rarely described in the case of pyrite and is supposed to follow a spinel-law (Gaubert 1928 and references therein). From the simulations, the (111) interface is likely to be defective due to the incompatibility of the sulfur network symmetry. The twin observed in Fig. 3 is an apparently smooth (111) surface, forming a lozenge in which the ideal smaller angle should be of 54.74º and the wider of 125.24º. The spinel-law does not seem applicable in this case and the intergrowing crystals do not enable to propose another theory. Further work on mathematical approaches on crystal growth and twinning based on rotational operators are under investigation.

IMPLICATIONS

Uncommon striated pyrite crystals have been identified in geothermal sites (e.g. Elba-Italy, Akita prefecture-Japan, Boyacá-Colombia and Cassandra-Greece). Elba is of peculiar interest because the island does not only record one of the largest pyrite crystals (Rickwood 1981) but also reveals rare ´negative´ striated pyritohedra co-growing with rare hematite specimens. Magnetism at ambient temperature on striated hematite is another singular feature which deserves to be studied in a future work, combining magnetometry, mass ions fluorescence technique more adapted for REEs and DFT studies including defect chemistry. MIO hematite is however fragile, with very thin layers, probably growing kinetically with defective interfaces from grain boundaries that might also affect magnetic properties. Crystal growth, striations, twinning and the straight relation between iron oxides and sulfides are part of the biotic or abiotic geochemistry history. The abiotic pyritization process has been linked to iron cycle and to the genesis of natural H_2 within the Earth´s crust (Arrouvel and Prinzhofer 2021). Persulfides, iron oxides and hydrogen play as well a key role in chemical origin of life renewing the interest to study pyritization processes and the co-growing of twinned anisotropic crystals.

ACKNOWLEDGEMENTS

C. Arrouvel gives a special thank to Elisabeth Lieutaud for her quest on the so-called *negative* pyrite; Krijn and his late wife Petra Tommel for donating *negative* pyrite and hematite from their collection. She thanks Claudine Arrouvel and Jacques Werckmann for the donation of pyrite crystals. The author is grateful to Dimat-INMETRO for giving access to the SEM equipment (FEI Magellan) and CBPF (Labnano and MatMult) for the use of SEM-XRD equipments with Raquel

Checca for assistance. She acknowledges Cenapad-SP for computational resources. She is grateful to the two anonymous reviewers for their inestimable comments helping to improve drastically the manuscript. The work has been done without any financial support.

REFERENCES CITED

Agata, T., and Adachi, M. (1995) Ilvaite from a serpentinized peridotite in the Asama igneous complex, Mikabu greenstone belt, Sambagawa metamorphic terrain, central Japan. Mineralogical Magazine, 59, 489-496.

Alfaro, C. Velandia, F., and Cepeda, H. (2005) Colombian Geothermal Resources. Proceedings World Geothermal Congress.

Alfaro–Valero, C.M., Rueda–Gutiérrez, J.B., Matiz–León, J.C., Beltrán–Luque, M.A., Rodríguez–Rodríguez, G.F., Rodríguez–Ospina, G.Z., González–Idárraga, C.E., and Malo–Lázaro, J.E. (2020) Paipa Geothermal System, Boyacá: Review of Exploration Studies and Conceptual Model. In: Gómez, J. and Pinilla–Pachon, A.O. (editors), The Geology of Colombia, Volume 4 Quaternary. Servicio Geológico Colombiano, Publicaciones Geológicas Especiales 38, 36 p. Bogotá.

Alfonso, D.R. (2010) Computational Investigation of FeS_2 Surfaces and Prediction of Effects of Sulfur Environment on Stabilities. Journal of Physical Chemistry C, 114, 8971-8980.

Alonso-Azcarate, J., Rodas, M., Fernandez-Diaz, L., Bottrell, S.H., Mas, J.R., and Lopez-Andres, S. (2001) Causes of variation in crystal morphology in metamorphogenic pyrite deposits of the Cameros Basin (N Spain). Geological Journal, 36, 159-170.

Aoki, Y., and Nakamuta, Y. (1984) Penetration twins of potassium chloride. Journal of Crystal Growth,67, 1984, Pages 579-586.

Arrouvel, C. (2021) Surfaces, Interfaces and Crystal Growth of Marcasite FeS_2, Materials Research, 24, e20200383.

Arrouvel, C., and Eon, J.G. (2019) Understanding the Surfaces and Crystal Growth of Pyrite FeS_2. Materials Research, 22, e20171140.

Arrouvel, C., and Prinzhofer, A. (2021) Genesis of natural hydrogen: New insights from thermodynamic simulations, International Journal of Hydrogen Energy, 46, 18780-18794.

Authier, A. (2013) Early Days of X-ray Crystallography, Oxford University press, UK, 2013, p373.

Bayliss, P. (1977) Crystal structure refinement of a weakly anisotropic pyrite. American Mineralogist, 62, 1168-1l72.

Bayliss, P. (1989) Crystal chemistry and crystallography of some minerals within the pyrite group, American Mineralogist, 74, 1168-1176.

Barnard, A. S., and Russo, S.P. (2009) Modelling nanoscale FeS_2 formation in sulfur rich conditions. Journal of Materials Chemistry, 19, 3389-3394.

Benvenuti, M., Dini, A., D'Orazio, M., Chiarantini, L., Corretti, A., and Costagliola, P. (2013) The tungsten and tin signature of iron ores from Elba Island (Italy): a tool for provenance studies of iron production in the Mediterranean Region. Archaeometry, 55, 479–506.

Bonev, I.K., Reiche, M., and Marinov, M. (1985) Morphology, perfection and growth of natural pyrite whiskers and thin platelets. Physics and Chemistry of Minerals, 12, 223–232.

Born M., and Huang K. (1954) Dynamical theory of crystal lattices. Oxford University Press, New York.

Cabá -Acevedo, M., Faber, M.S.,Tan, Y., Hamers, R.J., and Jin, S. (2012) Synthesis and Properties of Semiconducting Iron Pyrite (FeS_2) Nanowires Nanoletters , 12, 1977−1982.

Cabá -Acevedo, M., Liang, D., Chew, K.S., DeGrave, J.P., Kaiser, N.S., and Song Jin (2013) Synthesis, Characterization, and Variable Range Hopping Transport of Pyrite (FeS_2) Nanorods, Nanobelts, and Nanoplates. Acsnano 7, 1731–1739.

Couderc, J.-J., Bras, J., Fagot, M., and Levade, C. (1980) Étude par microscopie électronique en transmission de l'état de déformation de pyrites de différentes provenances. Bulletin de Minéralogie, 103, 547-557.

Dana, E S. (1903) The system of mineralogy of James Dwight Dana, 6th ed., 84 p. Wiley, New York.

de Leeuw, N.H., Parker, S.C., Sithole, H.M. and Ngoepe, P.E. (2000) Modeling the surface structure and reactivity of pyrite: Introducing a potential model for FeS_2. Journal of Physical Chemistry B, 104, 7969-7976.

Deville, E. and Prinzhofer, A. (2016) The origin of N_2-H_2-CH_4-rich natural gas seepages in ophiolitic context: A major and noble gases study of fluid seepages in New Caledonia. Chemical Geology, 440, 139-147.

Donnay, G., Donnay, J.D.H., and Iijima, S. (1977) A high-resolution electron micrograph of the twin boundary in pyrite. Acta Crystallographica, A 33, 622-626.

Drabek, M., and Rieder, M. (2005) Mineral Deposit Research: Meeting the Global Challenge. In: Proceedings of the Eighth Biennial SGA Meeting, Mao J., and Bierlein F.P: eds, Springer, Beijing, China, 111-113.

Dzade, N.Y., and de Leeuw, N.H. (2017) Periodic DFT+U investigation of the bulk and surface properties of marcasite (FeS_2). Physical Chemistry Chemical Physics, 19, 27478-27488.

Endo, Y., and Sunagawa, I. (1973) Positive and Negative Striations in pyrite. American Mineralogist, 58, 930-935.

Endo, Y. (1978) Surface Microtopographic Study of Pyrite Crystals. Bulletin of the Geological Survey of Japan, 29, 701–764.

Ennaoui, A., Fiechter, S., Pettenkofer, C., Alonsovante, N., Buker, K., Bronold, M., Hopfner, C., Tributsch, H. (1993) Iron disulfide for solar-energy conversion. Solar Energy Materials and Solar Cells, 29, 289-370.

Folk, R.L. (2005) Nannobacteria and the formation of framboidal pyrite: Textural evidence. Journal of Earth System Science, 114, 369-374.

Friedel, G. (1926). Leçons de Cristallographie. Paris: Berger-Levrault.

Gaubert, M.P. (1928) Sur un cristal de pyrite, maclé suivant la loi des spinelles. In: Bulletin de la Société française de Minéralogie, 51, 211-212.

Gibbons, G.S. (1967) Optical Anisotropy in Pyrite. American Mineralogist, 52, 359–370.

Goldschmidt , V. (1890) Index der Krystallformen der Mineralien: Zweiter Band. Springer-Verlag Berlin Heidelberg.

Gong, M., Kirkeminde, A., and Ren, S. (2013) Symmetry-Defying Iron Pyrite (FeS_2) Nanocrystals through Oriented Attachment. Scientific Report, 3, 2092.

Gronvold F., and Westrum Jr E.F. (1976) Heat capacities of iron disulfides: thermodynamics of marcasite from 5 to 700K, pyrite from 300 to 780K, and the transformation of marcasite to pyrite. Journal of Chemical Thermodynamics, 8, 1039-1048.

Hartman, P. (1963) Structure, growth and morphology of crystals. Zeitschrift für Kristallographie, 119, 65-78.

Hartman P., and Perdok, W.G. (1955) On the relations between structure and morphology of crystals. I. Acta Crystallographica. 8, 49-52

Huang, L.Y., and Meng, L. (2007) Effects of film thickness on microstructure and electrical properties of the pyrite films. Materials Science and Engineering B, 137, 310–314.

Hung, A., Muscat, J., Yarovsky, I., and Russo, S.P. (2002a) Density-functional theory studies of pyrite FeS_2 (111) and (210) surfaces. Surface Science, 520, 111-119.

Hung A, Muscat J, Yarovsky I, Russo SP. (2002b) Density-functional theory studies of pyrite FeS_2(100) and (110) surfaces. Surface Science, 513, 511-524.

Kougoulis Ch., Arvanitis A., Kolios N., Koutsinos S. , and Kougoulis J.-S. (2007) Geothermal exploration in the Sani - Afytos area of the Kassandra Peninsula (Chalkidiki Peninsula, Northern Greece). Bulletin of the Geological Society of Greece 40, 1162-1176.

Kresse, G., and Furthmüller, J. (1996) Efficiency of ab-initio total energy calculations for metals and semiconductors using a plane-wave basis set. Computational Materials Science, 6, 15-50.

Lippolt, H.J., Wernicke, R.S., and Bähr, R. (1995) Paragenetic specularite and adularia (Elba, Italy) : Concordant (U + Th) -He and K-Ar ages. Earth and Planetary Science Letters, 132, 43-51.

Liu, S., Wu, J., Yu, P., Ding, Q., Zhou, Z., Li, H., Lai, C.-C., Chueh, Y.L., Wang, Z.M. (2014) Phase-pure iron pyrite nanocrystals for low-cost photodetectors. Nanoscale Research Letters, 9, 549.

Liu, Z.-c., Zheng, Y.-j. (2011) Micaceous iron oxide prepared from pyrite cinders by hydrothermal method. Journal of Central South University of Technology, 18, 89–95.

Murowchick, J.B., and Barnes, H. (1986) Marcasite precipitation from hydrothermal solutions. Geochimica Cosmochimica Acta, 50, 2615-2629.

Murowchick, J.B., and Barnes, H.L. (1987) Effects of temperature and degree of supersaturation on pyrite morphology. American Mineralogist, 72, 1241-1250.

Nesbitt, H.W., Bancroft, G.M., Pratt, A.R., and Scaini, M.J. (1998) Sulfur and iron surface states on fractured pyrite surfaces. American Mineralogist, 83, 1067–1076.

Noorollahi, Y., Itoi, R., Fujii, H., and Tanaka T. (2007) GIS model for geothermal resource exploration in Akita and Iwate prefectures, northern Japan. Computers & Geosciences, 33, 1008–1021.

Pabst, A. (1971) Pyrite of unusual habit simulating twinning from the Green River Formation of Wyoming. American Mineralogist, 56, 133-145.

Rečnik, A., Zavašnik, J., Jin, L., Čobić, A., and Daneu, N. (2016) On the origin of 'iron-cross' twins of pyrite from Mt. Katarina, Slovenia. Mineralogical Magazine. 80, 937-948.

Rickard D. (2012) Sulfidic Sediments and Sedimentary Rocks. In: Developments in Sedimentology. Elsevier. 65, ch. 5, 195-231.

Rice, R.V., Cohen, A.J. (1958) A new method for orienting electron microscope replicas applied to twinned quartz. American Mineralogist, 43. 25-33.

Rickard, D. (2015) Pyrite A Natural History of Fool's Gold. Oxford University press, New York.

Rickwood, P.C. (1981) The largest crystals. American mineralogist, 66, 885-908.

Saccani, E., and Principi, G. (2016) Petrological and tectono-magmatic significance of ophiolitic basalts from the Elba Island within the Alpine Corsica-Northern Apennine system. Mineralogy and Petrology, 110, 713–730.

Roberts, D.M., Russek, S.E., and Stoldt, C.R. (2019) Synthetic iron pyrite across length scales: interfacial defects and macroscopic properties. CrystEngComm, 21, 3304-3312.

Savage, K.S., Stefan, D., and Lehner S.W. (2008) Impurities and heterogeneity in pyrite: Influences on electrical properties and oxidation products. Applied Geochemistry, 23, 103–120.

Schoonen, M.A.A., Barnes, H.L. (1991) Reactions forming pyrite and marcasite from solution: I. Nucleation of FeS_2 below 100ºC. Geochimica Cosmochimica Acta, 55, 1495–1504.

Skál , R., Císa ová, I., and Drábek, M. (2006) Inversion twinning in troilite. American Mineralogist, 91, 917-921.

Squadrone, S., Nurra, N., Battuello, M., Sartor, R.M., Stella, C., Brizio, P., Mantia, M., Pessani, D., and Abete, M.C. (2018) Trace elements, rare earth elements and inorganic arsenic in seaweeds from Giglio Island (Thyrrenian Sea) after the Costa Concordia shipwreck and removal. Marine Pollution Bulletin, 133, 88–95.

Sun, R., Chan, M.K.Y., and Ceder, G. (2011) First-principles electronic structure and relative stability of pyrite and marcasite: Implications for photovoltaic performance. Physical Review B, 83, 235311.

Tanelli, G., Benvenuti, M., Costagliola, P., Dini, A., Lattanzi, P., Maineri, C., Mascaro, I., and Ruggieri G. (2001) The iron mineral deposits of Elba Island: State of the art, Ofioliti, 26, 239-248.

Tasker, P.W. (1979) Stability of ionic crystal surfaces. Journal of Physics C: Solid State Physics, 12, 4977-4984.

Vedavathia, A., Reddy, Y.M., and Reddy, K.T.R. (2015) Effect of Precursor Concentration on Structural and Morphological Properties of Iron Pyrite Thin Films. Procedia Materials Science, 10, 279 – 284.

Yamada, S., Nanjo, J., Nomura, S., and Hara, S. (1979) Morphology of iron pyrite crystals. Journal of Crystal Growth , 46, 10-14.

Yang, S.-L., Yao, H.-B., Gao, M.-R., and Yu, S.-H. (2009) Monodisperse cubic pyrite NiS_2 dodecahedrons and microspheres synthesized by a solvothermal process in a mixed solvent: thermal stability and magnetic properties. CrystEngComm , 11, 1383–1390.

Watson, G.W., Kelsey, E.T., de Leeuw, N.H., Harris, D.J., and Parker, S.C. (1996) Atomistic simulation of dislocations, surfaces and interfaces in MgO. Journal of the Chemical Society, Faraday Transactions, 92,433-438.

White, J.S. Jr. (1973) Extreme symmetrical distortion of pyrite from Naica, Mexico. Mineralogical Record, 4, 267-270.

Wilkin, R.T, Barnes, H.L, and Brantley, S.L. (1995) The size distribution of framboidal pyrite in modern sediments: An indicator of redox conditions. Geochimica et Cosmochimica Acta, 60, 3897-3912.

Wulff, G. (1901) Zur Frage der Geschwindigkeit des Wachstums und der Auflösung der Krystallflagen. Zeitschrift Fur Kristallographie, 34,449-530.

Yu, B.-B., Zhang, X., Jiang, Y., Liu, J., Gu, L., Hu, J.-S. and Wan, L.-J. (2015) Solvent-Induced Oriented Attachment Growth of Air-Stable Phase-Pure Pyrite FeS_2 Nanocrystals. Journal of the American Chemical Society, 137, 2211−2214.

Zavrazhnov, A., Naumov, A., Kosyakov, A., Berezin, S.S., Volkov, V.V., and Sergeeva A.V. (2018) The Iron Sulfides Crystal Growth from the Halide Melts. Materials Research, 21, e20170648.

Zhang, Y. N., Law, M., and Wu, R.Q. (2015) Atomistic Modeling of Sulfur Vacancy Diffusion Near Iron Pyrite Surfaces. Journal of Physical Chemistry C, 119, 24859.

Zucchi, M. (2020) Faults controlling geothermal fluid flow in low permeability rock volumes: An example from the exhumed geothermal system of eastern Elba Island (northern Tyrrhenian Sea, Italy). Geothermics, 85, 101765.

List of figures

FIGURE 1. Photograph (by C. Arrouvel) and SEM image of cubic pyrite (origin unknown).

FIGURE 2. Photographs (by C. Arrouvel) and SEM images of natural pyritohedral pyrite a) positive striations (origin Peru) b) negative striations (Krijn Tommel donation, origin Italy).

FIGURE 3. Photographs (by C. Arrouvel) and SEM images of octahedral pyrite with a (111) twin, (Origin Peru). Note: the twin looks like Fig. 90 p.40 in Dana (1903)

FIGURE 4. XRD of cubic, positive and negative striated pyrite, V: Vaesite NiS_2, T: Troilite FeS.

FIGURE 5. Optimised grain boundaries in polyhedral representations a) (110) ; b) (111)

TABLE 1. Interatomic potentials for FeS_2

q (|e|)	Fe +2.0	S -1.0	
Buckingham potential	A (eV)	ρ (Å)	C (eV $Å^{-6}$)
Fe-S	94813.90	0.18125	0.0000
S-S	1777.08	0.33080	97.4915
Constant Force	k (eV)	r_0 (Å)	
S-S	8.44	2.23	
3-body potential	k (eV.rad^{-2})	θ_0	
S - S - Fe	12.5	109.503°	

Table 2. Attachment energies, surface energies and structure of the facets of Miller indices {hkl}.

Indices	Attachment energy (|eV|/at)	Surface energy unrelaxed (γ_{hkl}) (Jm^{-2})	Surface energy relaxed (γ_{hkl}) (Jm^{-2})	Unrelaxed Termination
(001) S	0.21	1.29	1.04	S1 S2
(110)	0.49	2.10	1.68	Fe S1 S2
(111) Fe*	1.31	4.78	3.22	Fe
(111) S*	1.31	4.89	3.38	S1 S2
(210)S	0.77	2.11	1.65	S1 S2
(210) Fe	0.62	2.13	1.66	Fe
(120) Fe	0.79	2.12	1.68	Fe
(120) S	1.78	4.81	2.92	S1 S2
(310) Fe*	0.70	1.90	1.47	Fe Fe S1 S2
(130) S	0.70	1.90	1.51	S1 S2
(311) S*	1.47	3.06	2.25	S1 S2

* from Arrouvel and Eon (2019)

Figures

FIGURE 1

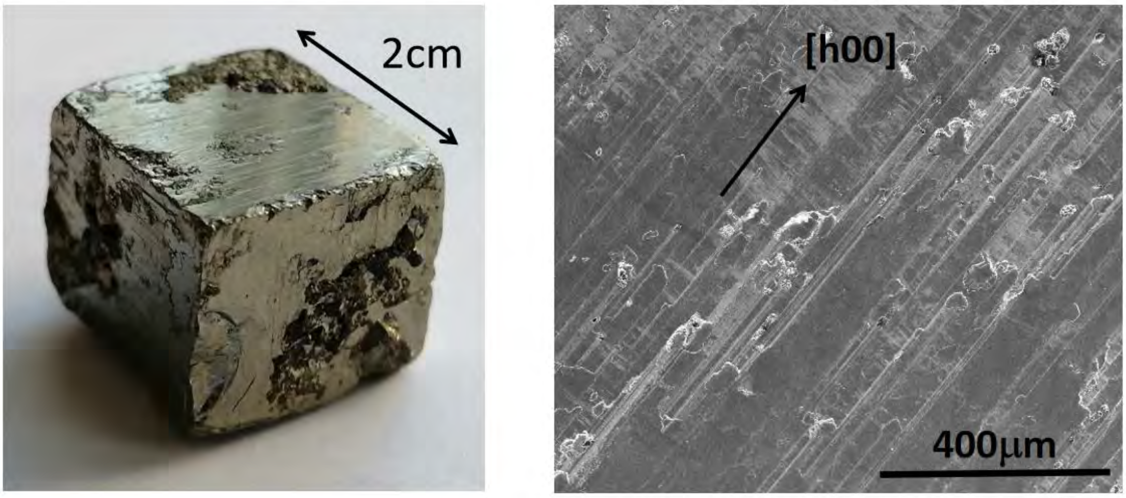

FIGURE 2

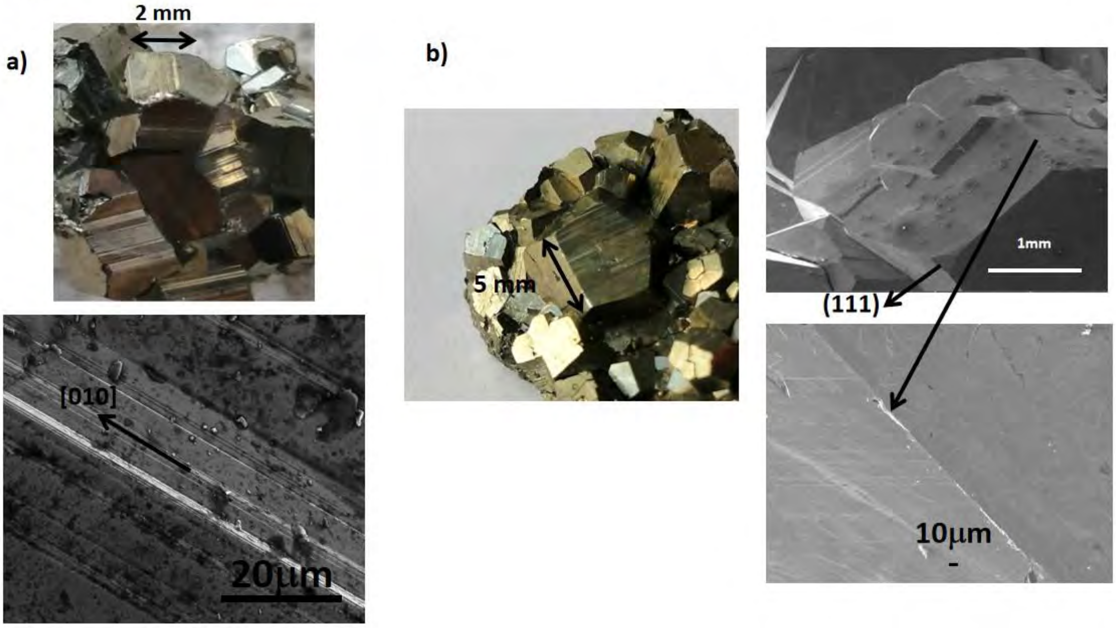

FIGURE 3

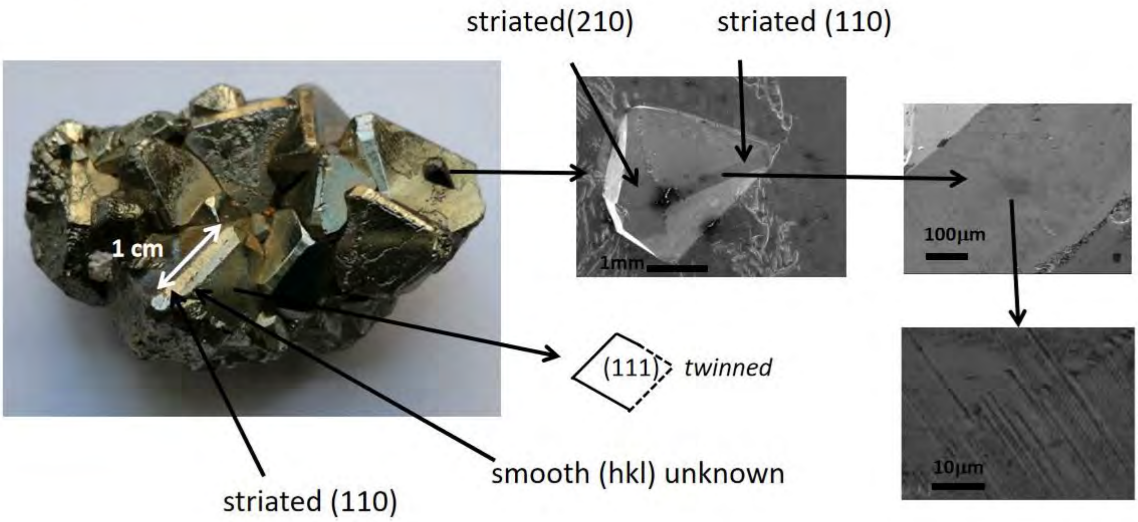

FIGURE 4

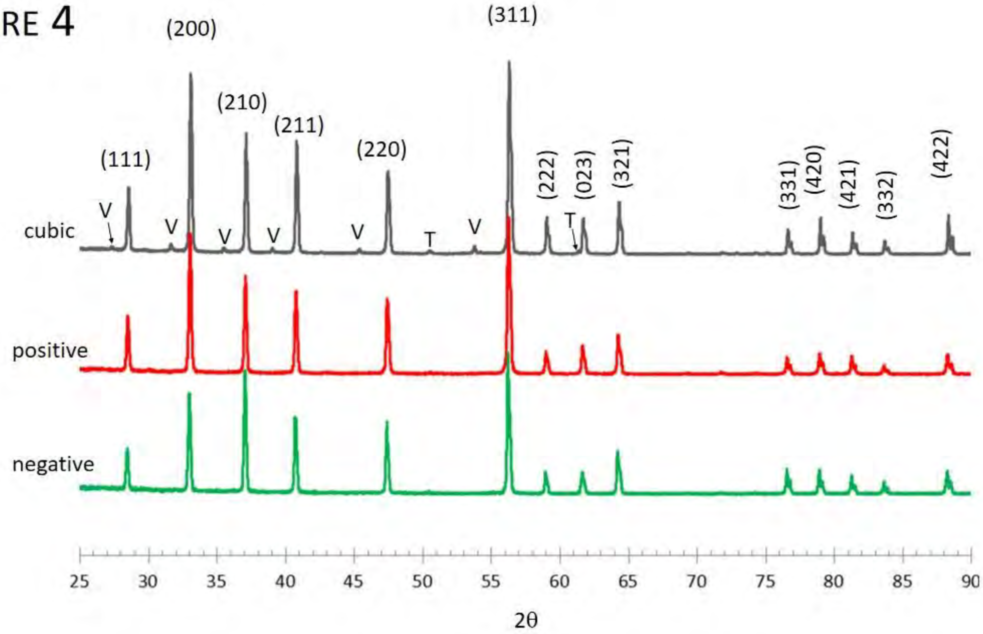

FIGURE 5

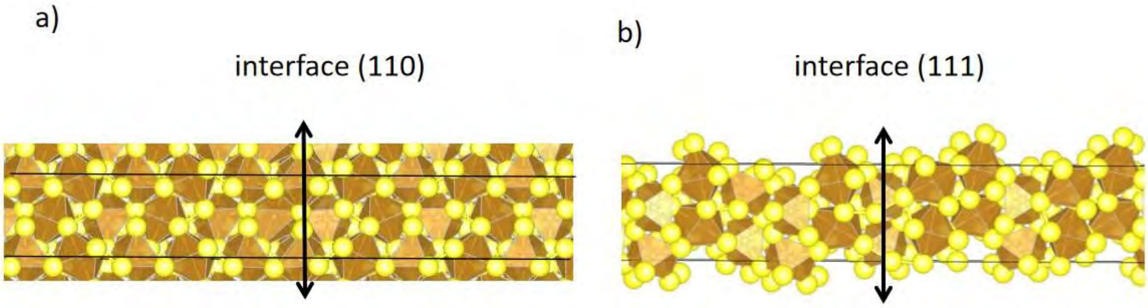

814

815

816